Local therapeutic platform prevents postsurgical GBM recurrence by diminishing GICs and reshaping immunosuppressive microenvironment

Mengxi Zhu [1,2,7], Mengting Yang [1,3,7], Rui Li[1,2,7], Xiwen Hu[1,2], Jiaxuan Chen[1,2], Limin Xu[1,2], Sunhui Chen[4], Tao Li[5], Jianxin Wang [6] ✉, Bin Zheng [1,2] ✉ & Huining He[1,2] ✉

Glioblastoma multiforme (GBM) is characterized by aggressive invasiveness and poor prognosis, and presents a significant clinical challenge due to incomplete surgical resection, poor blood–brain barrier penetration of therapeutic agents, and inevitable recurrence mainly driven by residual glioma-initiating cells (GICs) and an immunosuppressive microenvironment. Therefore, there is an urgent need to kill remaining GICs and reverse the immunosuppressive tumor microenvironment to prevent postoperative recurrence of GBM. Here, we design an injectable therapeutic platform that targets and kills remaining GICs and reverses the immunosuppressive microenvironment after postoperative resection to prevent the recurrence of GBM. This platform comprises GIC-targeting exosomes that carry siRNA for Notch1 and mitoxantrone to reduce the stemness of GICs and kill residual GICs and glioma cells, respectively, and an immune activator (interleukin-12), which can remodel the immunosuppressive tumor microenvironment, ultimately suppressing postoperative GBM relapse. Our work provides a perspective into the effective inhibition of postresection recurrence of GBM.

GBM, the most lethal type of brain tumor with a poor prognosis and a 5-year survival rate of less than 6%[1], accounts for approximately 48% of all primary malignant central nervous system (CNS) tumors[2]. For patients with GBM, the initial clinical intervention is surgical debulking, and chemoradiotherapy (CRT) is typically administered approximately one month after surgery[3–5]. This one-month post-operative interval represents a crucial period during which tumor recurrence may be triggered[6]. GBM recurrence can occur as a result of the difficulty incompletely removing the tumors[7]; in particular, residual GICs in deep intracranial locations of the brain are highly infiltrative and diffuse, leading to recurrence in almost all GBM patients[8]. Thus, targeted in situ eradication of residual GICs may be a promising therapeutic strategy against GBM recurrence.

[1]Tianjin Key Laboratory on Technologies Enabling Development of Clinical Therapeutics and Diagnostics, School of Pharmacy, Tianjin Medical University, Tianjin, China. [2]International Joint Laboratory of Ocular Diseases, School of Biomedical Engineering and Technology, Tianjin Medical University, Tianjin, China. [3]Department of Pharmacy, Tianjin First Central Hospital, Tianjin, China. [4]Shengli Clinical College of Fujian Medical University, Department of Pharmacy of Fujian Provincial Hospital & Fuzhou University Affiliated Provincial Hospital, Fuzhou, China. [5]Department of Neurosurgery, Tianjin Medical University General Hospital & Laboratory of Neuro-Oncology, Tianjin Neurological Institute, Tianjin, China. [6]Department of Pharmaceutics, School of Pharmacy, Fudan University & Key Laboratory of Smart Drug Delivery, Ministry of Education, Shanghai, China. [7]These authors contributed equally: Mengxi Zhu, Mengting Yang, Rui Li. ✉e-mail: jxwang@fudan.edu.cn; binzheng@tju.edu.cn; hehuining@tmu.edu.cn

GICs, a special aggressive population of cancer cells with self-renewal ability and multidirectional differentiation ability, are central to the recurrence of malignant glioma and therapeutic resistance[9,10]. Notch signaling, as an important mediator, is associated with stem cell self-renewal and therapeutic resistance, and evidence has shown that Notch1 is overexpressed in GICs and serves as a critical regulator in maintaining GIC stemness[11,12]. Therefore, specifically knocking down Notch1 expression via small interfering RNA (siRNA) may be an attractive approach for preventing GBM recurrence. Additionally, evidence has indicated that, compared with the first-line chemotherapy agent temozolomide (TMZ), mitoxantrone (MIT) has approximately 50 times stronger killing effects on GICs[13,14], triggering tumor cell immunogenic cell death (ICD) and inducing the maturation of dendritic cells (DCs)[15]. Codelivery of siNotch1 and MIT may both eliminate GICs and increase the expression of tumor-associated antigens, thus activating immunity. However, the poor stability and targeting of siRNA and MIT are the primary barriers to their application, and suitable vesicles that can be delivered into cells are needed[16]. Exosomes (exos) are natural nanomembrane vesicles that originate from endocytosis and are released into the extracellular environment following the fusion of multivesicular bodies (MVBs) with the plasma membrane[17]. Their nanoscale size, low immunogenicity and easy modification make exos excellent candidates as drug carriers[18]. Therefore, the co-laden exos were further surficially modified with targeted peptides (DVAP peptides have good affinity for GRP78, which is lowly expressed in normal cells and highly expressed in GICs and glioma cells[19]), with the goal of targeting the remaining GICs and glioma cells.

Another key factor for recurrence is the highly immune inhibitory tumor microenvironment in GBM, which inhibits effective immune surveillance by promoting the release of immune suppressors and altering the infiltration of CD4+ T and CD8+ T cells, DC cells, regulatory T cells (Treg cells) and myeloid-derived suppressor cells (MDSCs)[20,21]. Interleukin-12 (IL-12), a "master" immune-activating cytokine with potent tumor-suppressive activity, plays a crucial role in cancer immune surveillance[22]. IL-12 can activate T cells with persistent cytotoxic activity, improve antigen presentation, and reshape endogenous immunosuppressive cells in the tumor microenvironment; thus, it has emerged as an attractive candidate for cancer immunotherapy[23]. However, systemic IL-12 is poorly tolerated. As a result, a delivery method that increases IL-12 concentrations more selectively in the tumor environment without systemic toxicity is desirable[24].

Surgical resection is the initial clinical intervention measure for GBM patients, and the postoperative in situ drug delivery system (PIDDS) can be seamlessly integrated with the operation, filling the postoperative treatment interval, eliminating residual tumor cells, and effectively inhibiting recurrence[25,26]. In addition, PIDDS provides an effective delivery approach for therapeutic agents, which results in high levels of therapeutic accumulation in the tumor microenvironment, bypassing the blood–brain barrier, thereby reducing side effects[27,28]. The use of the Gliadel® wafer remains the sole FDA-approved PIDDS for GBM, although it is rarely used clinically due to complications[29]. Various formulations of intracavity delivery systems have been proposed, among which hydrogels with high biocompatibility and nonimmunogenicity have exhibited promising potential for use in biomedical applications[30].

In this work, we establish a therapeutic platform to serve as a drug reservoir for simultaneous delivery of VEMR (exosomes modified with DVAP targeted peptides carrying MIT and siNotch1 simultaneously, DVAP-Exo/MIT/siNotch1) and IL-12 (IL-12&VEMR@Gel). After intracavity injection, the cargoes are released from the prepared formulations in a sustained manner. VEMR target residual GICs and glioma cells in the resection cavity; subsequently, siNotch1 and MIT are released from exos and target to kill the GICs. Furthermore, MIT and IL-12 synergistically activate T cells and reshape the immunosuppressive microenvironment, thereby reducing glioma relapse (Fig. 1). In summary, the regression of glioma relapse following surgery may be achieved using a multifunctional exo-gel delivery system.

Results
Preparation and characterization of VEMR

First, we assessed the viability of exos as carriers for the simultaneous loading of MIT and siNotch1. Exos were isolated from the culture supernatant of RAW 264.7 cells via ultracentrifugation, DVAP peptides were modified on exos by click chemistry, and coincubation and transfection reagents (exofect) were performed simultaneously to load MIT and siNotch1 into exos (Fig. 2a). The TEM images in Fig. 2b, c showed that both the empty exos and VEMR exhibited a typical "disc" shape. Nano-particle tracking analysis (NTA) revealed that a peak particle diameter of empty exos was approximately 124 ± 2.55 nm, and the diameter of VEMR expanded to 136 ± 4.23 nm after encapsulation of the two therapeutic agents (Fig. 2d, e). Typical exo markers (CD9, TSG101, and CD63) were detected via Western blotting and enriched in exos (Fig. 2f). TAMRA fluorescent dye was subsequently used to label the DVAP-targeting peptides, and the TAMRA-VE (TAMRA-DVAP-Exo) positivity rate was detected via flow cytometry (FCM) to verify whether the chemical coupling of targeted peptides and exos was successful. The results shown in Fig. 2g revealed that approximately 88.6% of the exos had fluorescent signals, demonstrating successful coupling of DVAP to the exos. These results indicated that the successful extraction of exos and the loading of MIT and siRNA did not notably alter exo morphology or physicochemical properties.

Next, we compared the encapsulation efficiency of MIT among three methods: electroporation, coincubation followed by transfection, and simultaneous coincubation and transfection. As shown in Fig. 2h and Table S1, the loading efficiency of MIT in exos was approximately 21%; thus, we chose the simultaneous coincubation and transfection method for subsequent experiments, and the efficiency of siRNA loading into exos by this method was approximately 72%. Furthermore, we investigated the release of MIT from VEMR at pH 5.5 and 7.4. As shown in Fig. 2i, MIT release occurred faster within the first 12 h but then slowed, and the release rates were approximately 74.16% (pH 5.5) and 52.27% (pH 7.4) at 48 h, indicating that more MIT was released under acidic conditions. One of the primary challenges in the application of siRNAs is their easy degradation by nucleases. To assess the protective effect of exos against siRNAs, the degradation of different samples incubated with RNase A at different time points was determined. The results (Fig. 2j) revealed that free siRNAs were mostly degraded at 30 min and completely degraded at 60 min, and the degradation of siRNAs in EMR was similar to that of free siRNAs when Triton X-100 was added; however, siRNAs in EMR without Triton X-100 exhibited little degradation at 120 min, indicating that exos had a good protective effect on siRNAs, which were not easily degraded by nucleases. In summary, these results confirmed the feasibility of coloading MIT and siNotch1 into exos.

Gel and VEMR@Gel were subsequently prepared and characterized (Figs. 2k–m and S1). The results revealed that the gel was liquid at low temperature (4 °C) and became solid at 37 °C (Fig. 2k), and the viscosity of gel and VEMR@Gel decreased with increasing shear rate (Fig. 2l), which indicated that they experienced shear thinning. In addition, the storage modulus (G′) of gel and VEMR@Gel was much greater than the loss modulus (G″) with increasing temperature, demonstrating that the solid hydrogel gradually formed (Fig. 2m). SEM of gel revealed a porous morphology; after loading with VEMR, fewer pores formed in VEMR@Gel, indicating that VEMR was loaded into the porous structure of the gel, and the hemolysis rate of the gel was 0.58%, which met the requirements of medical materials (Fig. S1). Furthermore, the exos released from the gel were investigated. Exos were labeled with DiI, then loaded into the gel, and the artificial cerebrospinal fluid was used as the release medium. 3D layer scanning was
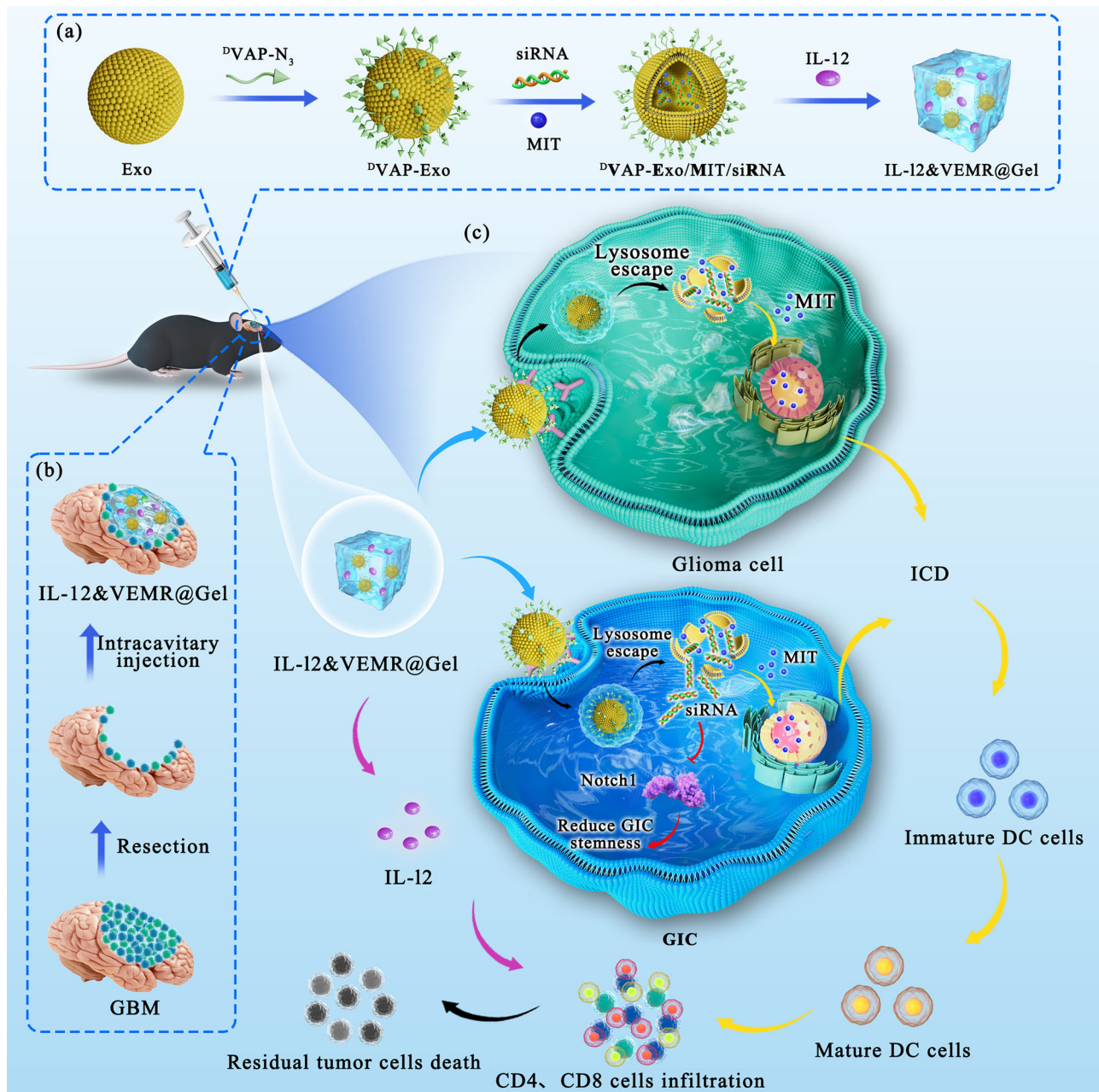
Fig. 1 | Intracavity-injected hydrogel system for preventing postoperative glioblastoma relapse. a Schematic illustration of the preparation of the exo-gel delivery system. **b**, **c** Schematic illustration of delivering exo-gel delivery system in resection cavity that kills remaining GICs and glioma cells, and reverses the immunosuppressive microenvironment to prevent recurrence of GBM.

performed via a laser confocal microscope, the results demonstrated that >80% exos could be released from the gel in 24 h (Fig. S2).

In vitro targeting and cellular uptake of VEMR

Immunomagnetic bead sorting was used to obtain U87 GICs, and Western blotting (Fig. S3a) revealed that CD133 and Nestin (stem cell markers), and Notch1 and Hes1 (Notch1 pathway-related proteins) were highly expressed in U87 GICs. Similarly, the immunofluorescence staining results (Fig. S3b) revealed that U87 GICs exhibited elevated expression of CD133 and Notch1. The above results suggested that U87 GICs were successfully sorted.

To investigate the targeting ability of the ^{D}VAP peptide, exos and ^{D}VAP-exos (VE) were labeled with DiI and subsequently incubated with U87 cells and U87 GICs (GRP78 positive) and HA1800 cells (a normal astrocyte with negative expression of the GRP78 protein).

Laser confocal microscopy revealed that the fluorescence intensities of VE and VEMR in U87 cells and U87 GICs were stronger than those in free exos (Fig. 3a–c, f), but their fluorescence signals were weaker when free ^{D}VAP targeting peptides were added in advance, indicating that exos were more likely to target glioma cells and GICs after targeted peptide modification and that free ^{D}VAP peptides could competitively bind to GRP78 to block VE targeting glioma cells and GICs. Moreover, almost no significant changes in fluorescence signal intensity were detected between the VE and VEMR groups, demonstrating that loading MIT and siRNA had little influence on the targeting ability of the exo delivery system. Next, the cellular uptake of this delivery system in U87 cells and U87 GICs was investigated. As shown in Fig. 3d, e, g–j, almost no fluorescence signals were detected in the PBS, siRNA and MIT groups, whereas few red and green fluorescence signals were detected in the EMR group. Stronger
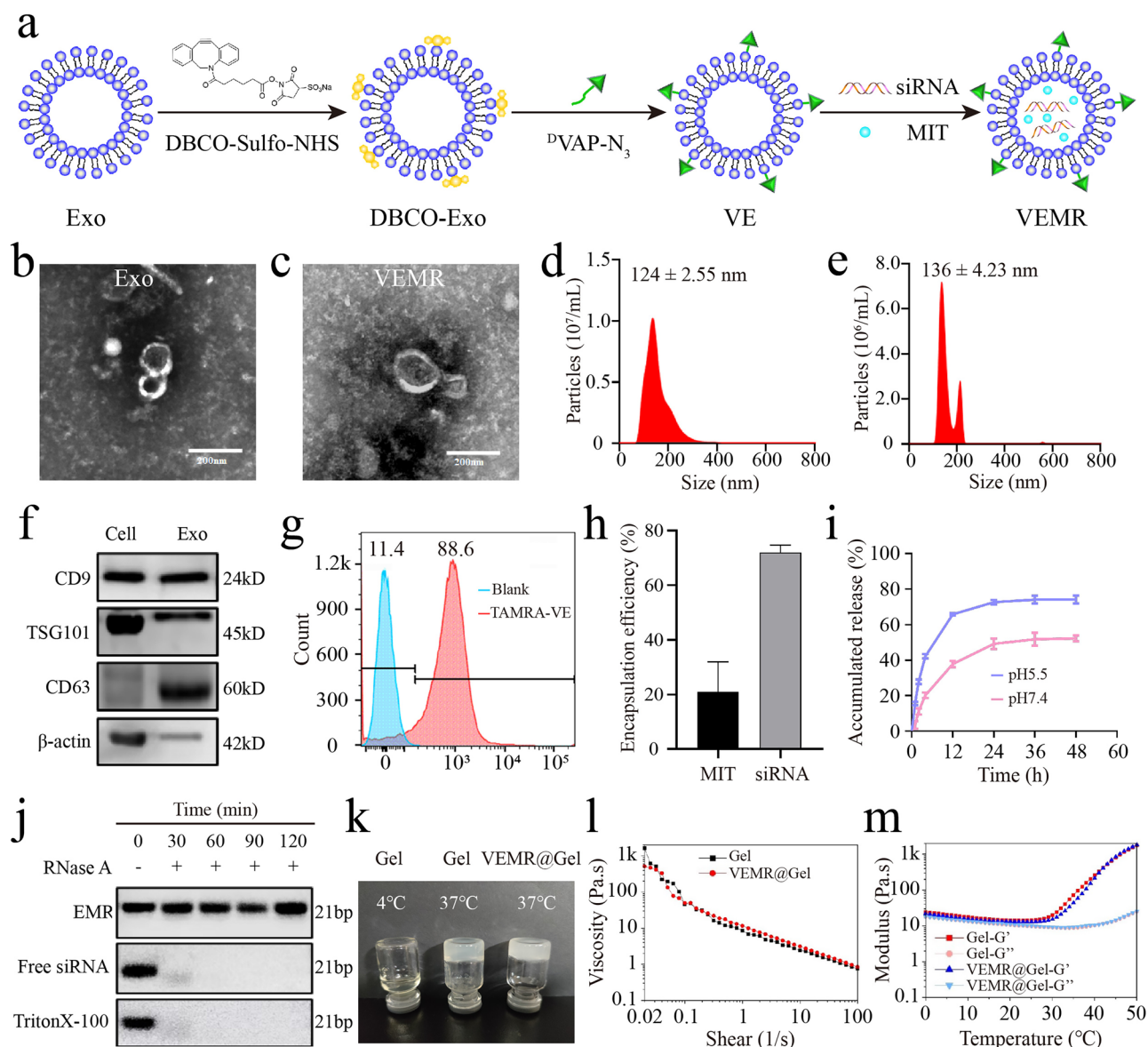
Fig. 2 | Characterization of the exo-based drug delivery system. a Schematic illustration of the preparation of the exo delivery system. **b, c** Representative TEM image of exos (**b**) and VEMR (**c**). **d, e** The size of exos (**d**) and VEMR (**e**). **f** Western blotting analysis of CD9, TSG101 and CD63 expression in exos. **g** Flow analysis diagram of ^{D}VAP targeting peptides modified exos. **h** The encapsulation rates of MIT and siRNA in VEMR ($n = 3$ independent experiments). Data are presented as mean ± SD. **i** Release curves of MIT in VEMR at pH 5.5 and 7.4 ($n = 3$ independent experiments). **j** Agarose gel electrophoresis image of siRNA incubated with or without RNase A at different time. **k** The temperature-sensitive properties of gel and VEMR@Gel at 4 °C and 37 °C. **l** The viscosity changes of gel and VEMR@Gel. **m** The storage modulus (G') and loss modulus (G'') of gel and VEMR@Gel in different temperature.

fluorescence signals for both channels were detected in the VEMR group. In other words, free siRNAs were minimally taken up by cells, whereas more siRNAs and MIT loaded into VE were internalized into cells, suggesting that exos modified with ^{D}VAP peptides could better promote the cellular uptake of drugs.

To elucidate the cellular uptake mechanism of targeted exos, U87 cells and U87 GICs were treated with various endocytosis inhibitors or maintained at 4 °C for incubation. Compared with control group, only a few red fluorescence signals were detected in the groups treated with amiloride (a macropinocytosis inhibitor), dynasore (a dynamin inhibitor) or incubated at 4 °C, whereas many red fluorescence signals were detected in the groups incubated with chlorpromazine (a clathrin inhibitor) and M-β-CD (a caveolin inhibitor), suggesting that the cellular uptake mechanism of targeted exos involved endocytosis mediated by dynamin, macropinocytosis and energy-dependent pathways

(Fig. 4a, b). Exos endocytosed into cells may participate in the endosome–lysosome pathway. To investigate whether drugs can escape from lyso/endosomes, we studied the colocalization of siRNAs and MIT with lyso/endosomes. As shown in Fig. 4c, after drugs were internalized into U87 cells at 2 h, the green, red and purple fluorescence exhibited a large amount of overlap. The colocalization coefficient of siRNA and lyso/endosomes was 0.97, and that of MIT and lyso/endosomes was 0.64. However, the overlap fluorescence gradually decreased with increasing time. At 8 h, the colocalization coefficient between siRNA and lyso/endosomes was 0.73, and that between MIT and lyso/endosomes was 0.39. The colocalization of siRNA, MIT and lyso/endosomes was similar in U87 GICs at 2 h and 8 h (Figs. 4d and S4–6), indicating that most of the siRNAs and MIT entered the lyso/endosomes and then escaped from the lyso/endosomes over time.
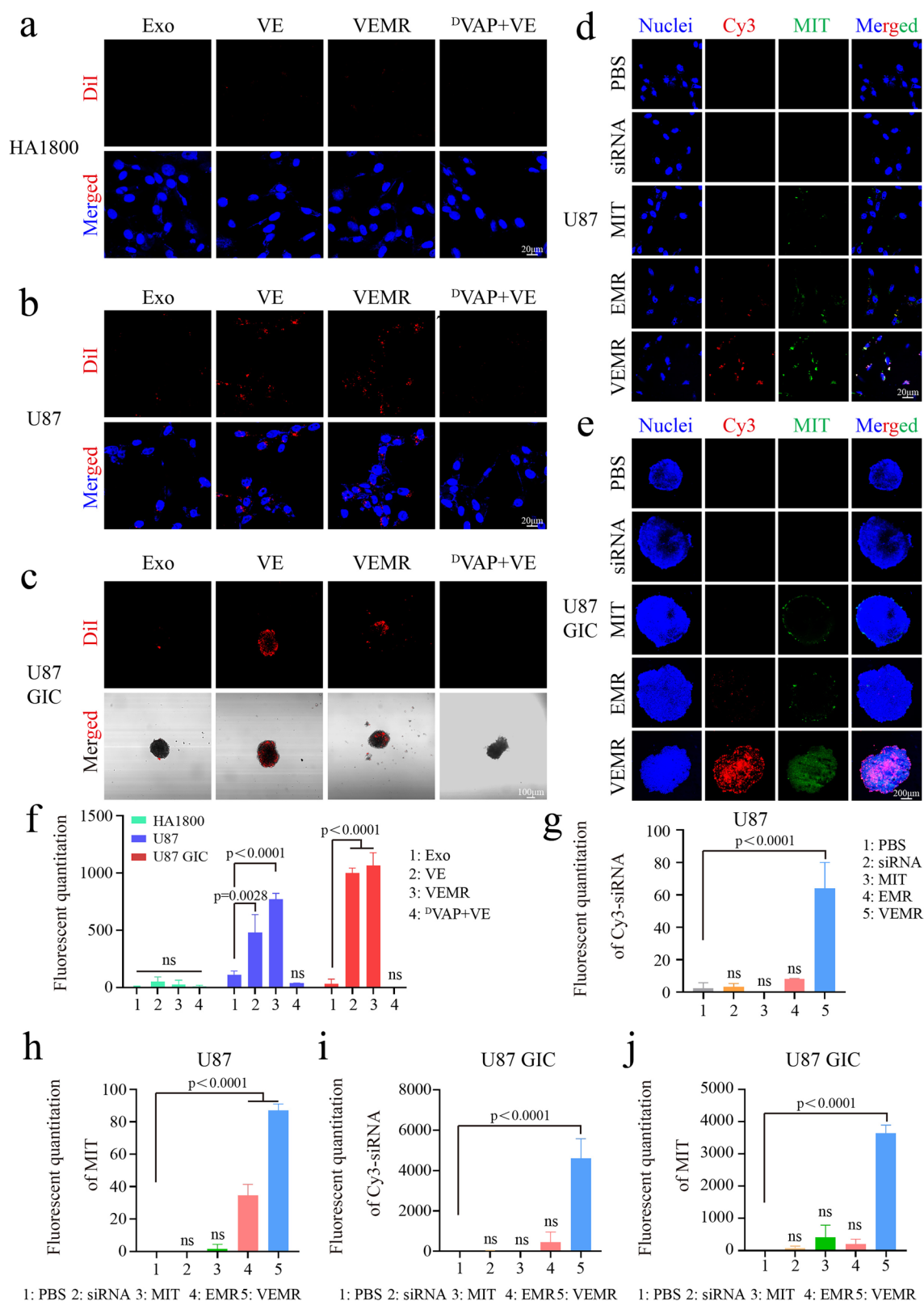
Fig. 3 | Targeting and uptake of the exo-based drug delivery system. a–c In vitro cellular targeting of exos, VE, VEMR, ^{D}VAP peptides and VE in HA1800 cells (**a**), U87 cells (**b**) and U87 GICs (**c**). Exos were labeled with DiI (red), cell nucleus was labeled with DAPI (blue). **d, e** In vitro cellular uptake of PBS, siRNA, MIT, EMR, and VEMR in U87 cells (**d**) and U87 GICs (**e**). Cell nucleus was labeled with DAPI (blue), siNotch1 was labeled with Cy3 (red), and MIT was green fluorescence. **f** Quantification of targeting in HA1800 cells (**a**), U87 cells (**b**) and U87 GICs (**c**) ($n = 3$ independent experiments). One-way ANOVA test was applied. Data are presented as mean ± SD. **g–j** Quantification of cellular uptake of siRNA and MIT in U87 cells (**d**) and U87 GICs (**e**) ($n = 3$ independent experiments). One-way ANOVA test was applied. Data are presented as mean ± SD.
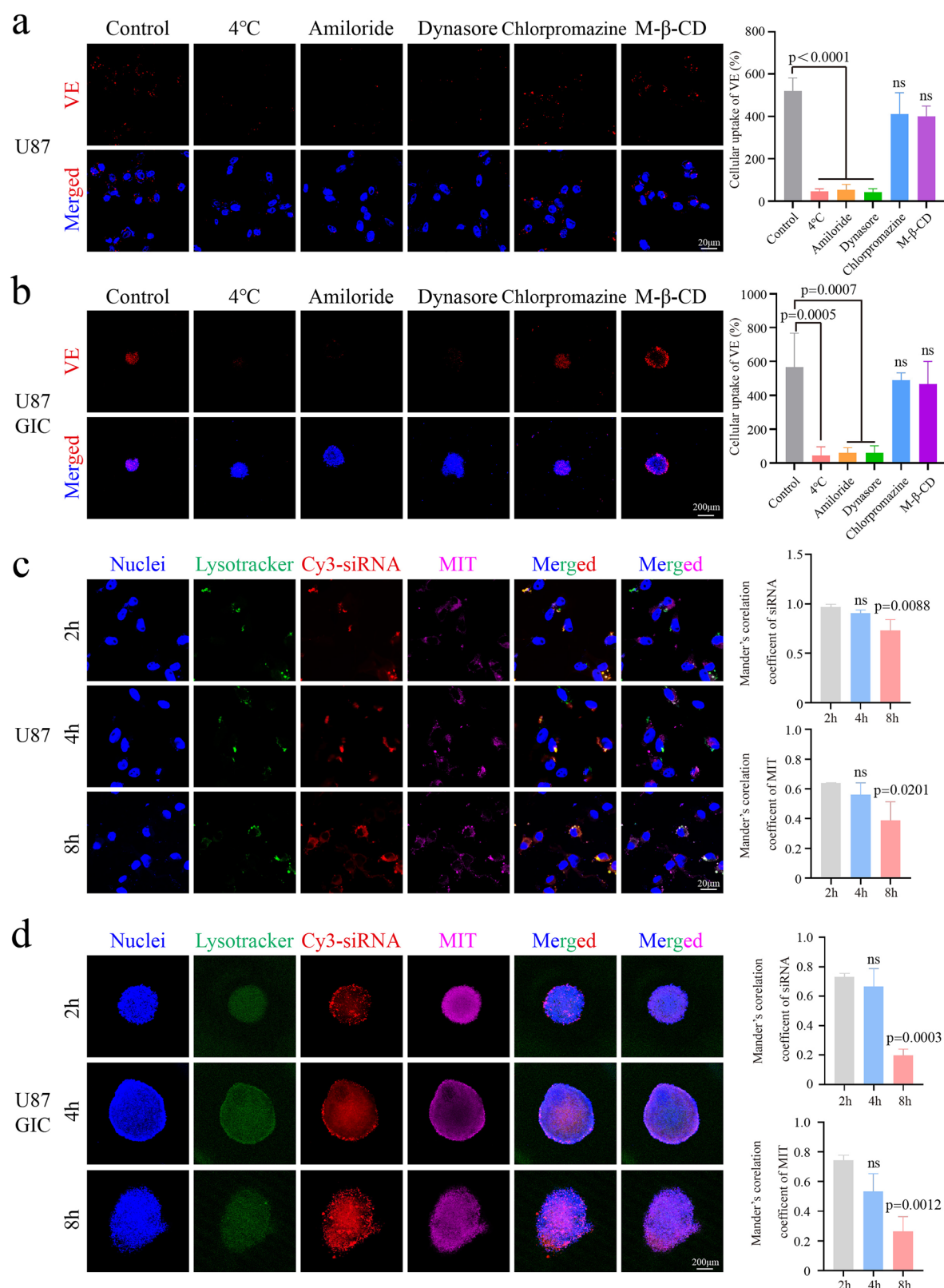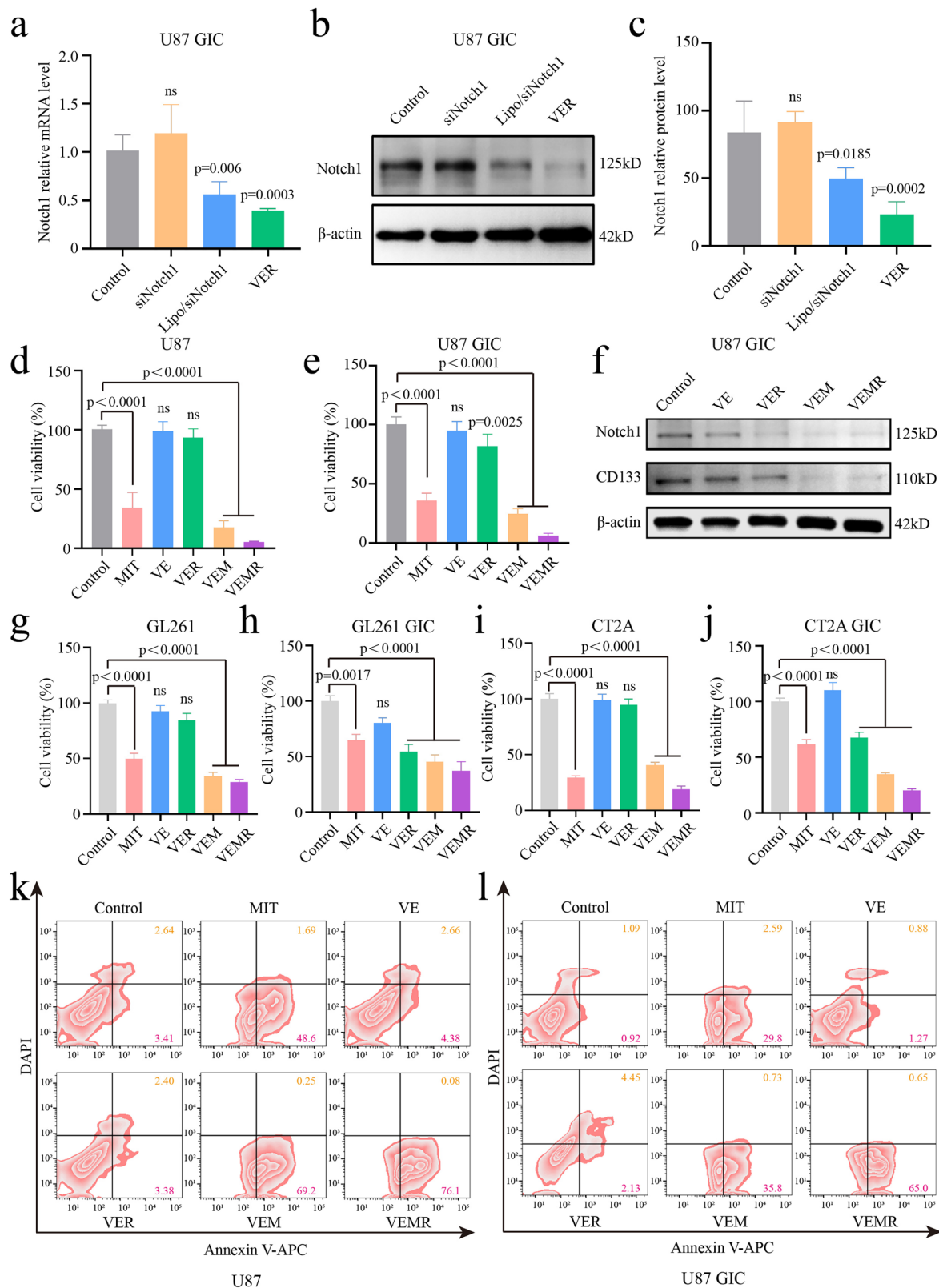
Fig. 4 | Cellular uptake mechanisms of the exo delivery system. a, b After treating U87 cells (**a**) and U87 GICs (**b**) with different endocytosis inhibitors (4 °C, amiloride, dynasore, chlorpromazine, M-β-CD), the CLSM images of their co-culture with VE for 2 h were obtained ($n = 3$ independent experiments). One-way ANOVA test was applied. Data are presented as mean ± SD. Exos were labeled with DiI (red), and cell nucleus was labeled with Hoechst 33342 (blue). **c, d** CLSM images of U87 cells (**c**) and U87 GICs (**d**) incubated with VEMR for 2, 4 and 8 h ($n = 3$ independent experiments). One-way ANOVA test was applied. Data are presented as mean ± SD. Cell nucleus was labeled with Hoechst 33342 (blue), lyso/endosomes were labeled with LysoTracker (green), siNotch1 was labeled with Cy3 (red), and MIT was purple fluorescence.

Synergistic antitumor efficacy of VEMR in vitro

To evaluate the biosafety of exos, HA1800 and U87 cells were exposed to increasing concentrations of exos. As shown in Fig. S7a, b, the cell viability of both HA1800 and U87 remained above 80% even at the highest concentration tested (100 µg/mL), indicating that the exos were safe. In addition, the safety of MIT in different samples was also tested to determine the optimal dosage concentration, and Fig. S7c

indicated that as the concentration increased, the viability of U87 cells decreased, and a final concentration of 5 µg/mL was chosen for further studies.

Furthermore, the antitumor effects of VEMR in glioma cells and GICs were investigated in vitro. First, the silencing effects of siNotch1 in U87 GICs were detected at mRNA and protein levels (Fig. 5a–c). Compared with the control group, the mRNA level of Notch 1 in U87

Fig. 5 | In vitro therapeutic effects of exo delivery system. a RT-qPCR was used to detect Notch1 mRNA level in U87 GICs incubated with PBS, siNotch1, lipo/siNotch1 and VER for 48 h ($n = 5$ independent experiments). One-way ANOVA test was applied. Data are presented as mean ± SD. **b** Western blotting analysis of Notch1 expression in U87 GICs incubated with PBS, siNotch1, lipo/siNotch1 and VER for 48 h. **c** Quantification of Notch1 expression in (**b**) ($n = 4$ independent experiments). One-way ANOVA test was applied. Data are presented as mean ± SD. **d**, **e** Cell viability of U87 cells (**d**) and U87 GICs (**e**) incubated with PBS, MIT, VE, VER, VEM, and VEMR for 48 h ($n = 5$ independent experiments). One-way ANOVA test was applied. Data are presented as mean ± SD. **f** Western blotting analysis of Notch1 and CD133 expressions in U87 GICs incubated with PBS, VE, VER, VEM and VEMR for 48 h. **g**–**j** Cell viability of GL261 cells (**g**), GL261 GICs (**h**), CT2A cells (**i**), CT2A GICs (**j**) incubated with PBS, MIT, VE, VER, VEM, and VEMR for 48 h ($n = 5$ independent experiments). One-way ANOVA test was applied. Data are presented as mean ± SEM. **k**, **l** Cell apoptosis of U87 cells (**k**) and U87 GICs (**l**) incubated with PBS, MIT, VE, VER, VEM and VEMR for 36 h.

GICs treated with ᴰVAP-Exo/siNotch 1 (VER) was reduced by 60%. Similarly, the protein expression level of Notch 1 was significantly downregulated (Fig. 5b, c), which was comparable to that in the positive control group (lipo/siNotch 1), whereas the protein expression level of Notch 1 in free siNotch 1 was not significantly changed, demonstrating that VER could effectively silence the target gene and inhibit the expression of Notch 1 in vitro. Furthermore, the proliferation and apoptosis of glioma cells and GICs were assessed through CCK8 and FCM assays to evaluate the therapeutic effects of the exo delivery system in vitro. Cell viability was significantly lower in the VEMR group (Figs. 5d, g, i and S8a) than that in the control group, but no substantial difference in cell survival was observed between the VEMR and VEM groups. However, the cell survival rates of the VER and VEM groups decreased by 18% and 75% in U87 GICs, 37% and 47% in U251 GICs, 46% and 55% in GL261 GICs, and 32% and 65% in CT2A GICs, respectively. Moreover, the cell survival rates in the VEMR group decreased by approximately 94% in U87 GICs, 49% in U251 GICs, 63% in GL261 GICs, and 80% in CT2A GICs, respectively (Figs. 5e, h, j and S8b). One possible reason for these differences is that the expression of Notch1 was low in glioma cells but high in GICs.

An Annexin V-APC/DAPI assay was performed to evaluate the apoptosis of glioma cells and GICs (Figs. 5k, l and S9–S12). In U87 cells (Figs. 5k and S9a), compared with the control group (4.86%), the apoptosis rates in both VE (5.22%) and VER (4.41%) groups did not significantly differ, whereas the apoptosis rates in the VEM and VEMR were 62.73% and 69.44%, respectively. In U87 GICs (Figs. 5l and S9b), compared with the control group (2.03%), the apoptosis rate in the VE group (2.87%) was not significantly different, whereas the apoptosis rates in the VER, VEM and VEMR groups were 8.13%, 35.06% and 64.85%, respectively. The apoptosis rates of U251 cells, GL261 cells, and CT2A cells as well as U251 GICs, GL261 GICs, and CT2A GICs were similar to those of U87 cells and U87 GICs (Figs. S10–S12); these results indicated that the exo delivery system had significant antitumor effects in vitro. Moreover, Western blotting revealed that, compared with control group, VEMR significantly decreased the expression levels of CD133 and Notch1 (Figs. 5f and S13), demonstrating that VEMR significantly reduced the stemness of U87 GICs and GL261 GICs. Taken together, VEMR successfully delivered siNotch1 and MIT into tumor cells to suppress proliferation and promote the apoptosis of GICs and glioma cells, subsequently suppressing the expression of the Notch1 protein to reduce GIC stemness. Additionally, synergistic treatment achieved better results than monotherapy did.

In vivo antitumor efficacy of intratumorally injected IL-12&VEMR

Encouraged by the above results, we further evaluated the therapeutic efficacy of the intratumoral injection of IL-12&VEMR. To establish the GL261 orthotopic glioma model, as depicted in Fig. 6a, luciferase-expressing GL261 (Luc-GL261) cells were implanted into the brains on day 0, and the mice underwent imaging using IVIS to measure glioma growth. On day 12 after being inoculated with Luc-GL261 cells, the mice were allocated into eight groups of different formulations (control, MIT, VER, VEM, EMR, VEMR, IL-12, and IL-12&VEMR). Throughout the therapeutic process, tumor growth and variations in body mass were closely monitored and recorded continually. Within the first three days

after each formulation was injected, there was a slight decrease in tumor growth among all treatment groups; however, one week after treatment, compared with the control group, the IL-12&VEMR group exhibited notable tumor suppression (Fig. 6b, c), and the median survival time of mice was significantly prolonged (Fig. 6d). Twenty-one days post-inoculation, mouse brain tumor tissues were harvested and sectioned for hematoxylin-eosin (H&E) staining to facilitate visualization under a microscope. The results revealed that maximal tumor growth suppression was observed in the IL-12&VEMR group among all treatment groups (Fig. 6e, g). TUNEL assays were conducted to detect apoptosis in all the experimental groups, and the green fluorescence signals were the weakest in the control group, but greatest in the IL-12&VEMR group compared with those in other groups (Fig. 6f, h), indicating that treatment with IL-12&VEMR could induce extensive apoptosis of tumor cells. To further assess the biocompatibility, body weight, serum indices (i.e., ALT, AST, BUN, and CRE), and H&E staining of major organs (including heart, liver, spleen, lung, and kidney) were analyzed (Fig. S14). Comparisons between the treatment groups and the control group revealed no significant differences, demonstrating that this exo delivery system had excellent biocompatibility with minimal toxicity.

Therapeutic effects of exo-gel delivery system on glioma relapse model

Surgical operation remains the preferred clinical approach for treating GBM patients, especially in cases involving more advanced tumor stages[31]. The effectiveness of postsurgery treatment options featuring close clinical correlation was evaluated using a personalized multifunctional exo-gel delivery system. To this end, visible gliomas were excised surgically from the mice on the 12th day after they were inoculated with Luc-GL261 cells (Fig. 7a). After surgical removal, mice were randomly assigned to seven groups, and the resection cavities were injected with each hydrogel-mediated treatment (the control group received surgical resection without hydrogel treatment). High signal intensities were observed in the control group and Gel group, whereas only a few were observed in the IL-12&VEMR@Gel group, indicating that IL-12&VEMR@Gel strongly inhibited GBM relapse (Fig. 7b, c). Murine resection cavities injected with EMR@Gel, VEMR@Gel and IL-12@Gel moderately inhibited tumor growth, prolonging the median survival duration to 25, 30 and 64 days, respectively, compared with the 16 days observed in the control group. The IL-12&VEMR@Gel group exhibited notable inhibition of tumor growth, with an extension in survival to 180 days (Fig. 7d). On the 30th day after tumor cell inoculation, the mice whose tumors excised were euthanized, and brain tumor tissues were harvested. H&E staining of tumor-bearing brain sections revealed that the fewest tumors were present in the IL-12&VEMR@Gel group (Figs. 7e and S15a). Additionally, extensive numbers of apoptotic cells were detected in TUNEL-stained tumor-bearing brain slices from the IL-12&VEMR@Gel group (Figs. 7f and S15b).

Based on the above experimental results, the therapeutic effects of this multifunctional exo-gel delivery system on a CT2A orthotopic glioma model were also investigated. Luciferase-expressing CT2A (Luc-CT2A) glioma cells were implanted into the brains on day 0, and the mice underwent imaging using an IVIS to determine glioma
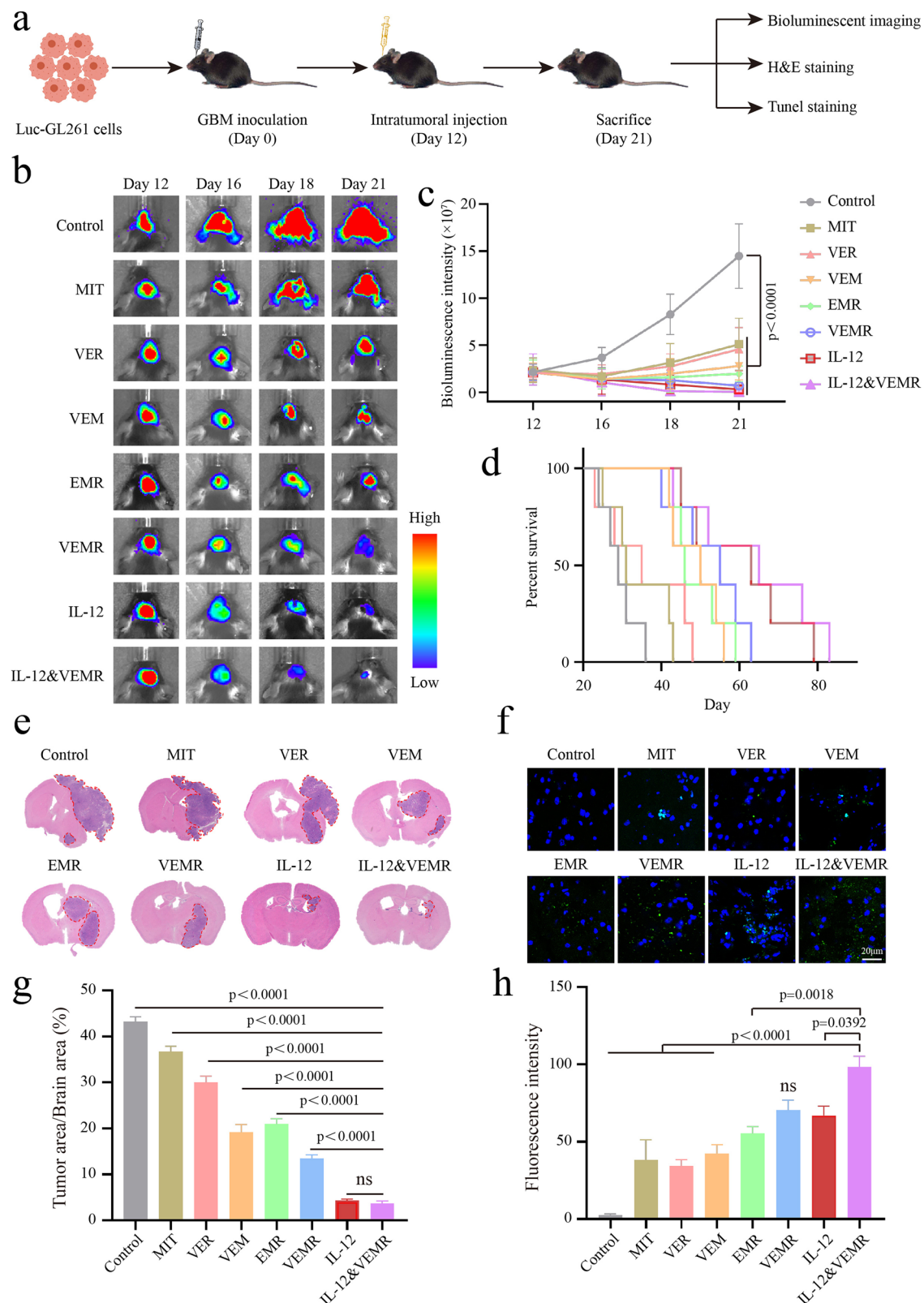
Fig. 6 | In vivo therapeutic therapy of different treatments on GBM. a Timeline schematic of the animal experiment. **b** Luminescence images of orthotopic Luc-GL261 GBM tumor-bearing mice following different treatments monitored on day 12, 16, 18, and 21. **c** Quantified signal intensity of (**b**) ($n = 5$ mice per group). Two-way ANOVA test was applied. Data are presented as mean ± SD. **d** Survival analysis of mice in each group ($n = 5$ mice per group). **e** Representative H&E images of the orthotopic GBM tumors after the indicated treatments. **f** TUNEL staining of brain tissue sections obtained from mice tumors after treatments. **g** Quantification of tumor area of (**e**) ($n = 3$ mice per group). One-way ANOVA test was applied. Data are presented as mean ± SD. **h** Fluorescence quantification of (**f**) ($n = 5$ mice per group). One-way ANOVA test was applied. Data are presented as mean ± SEM.
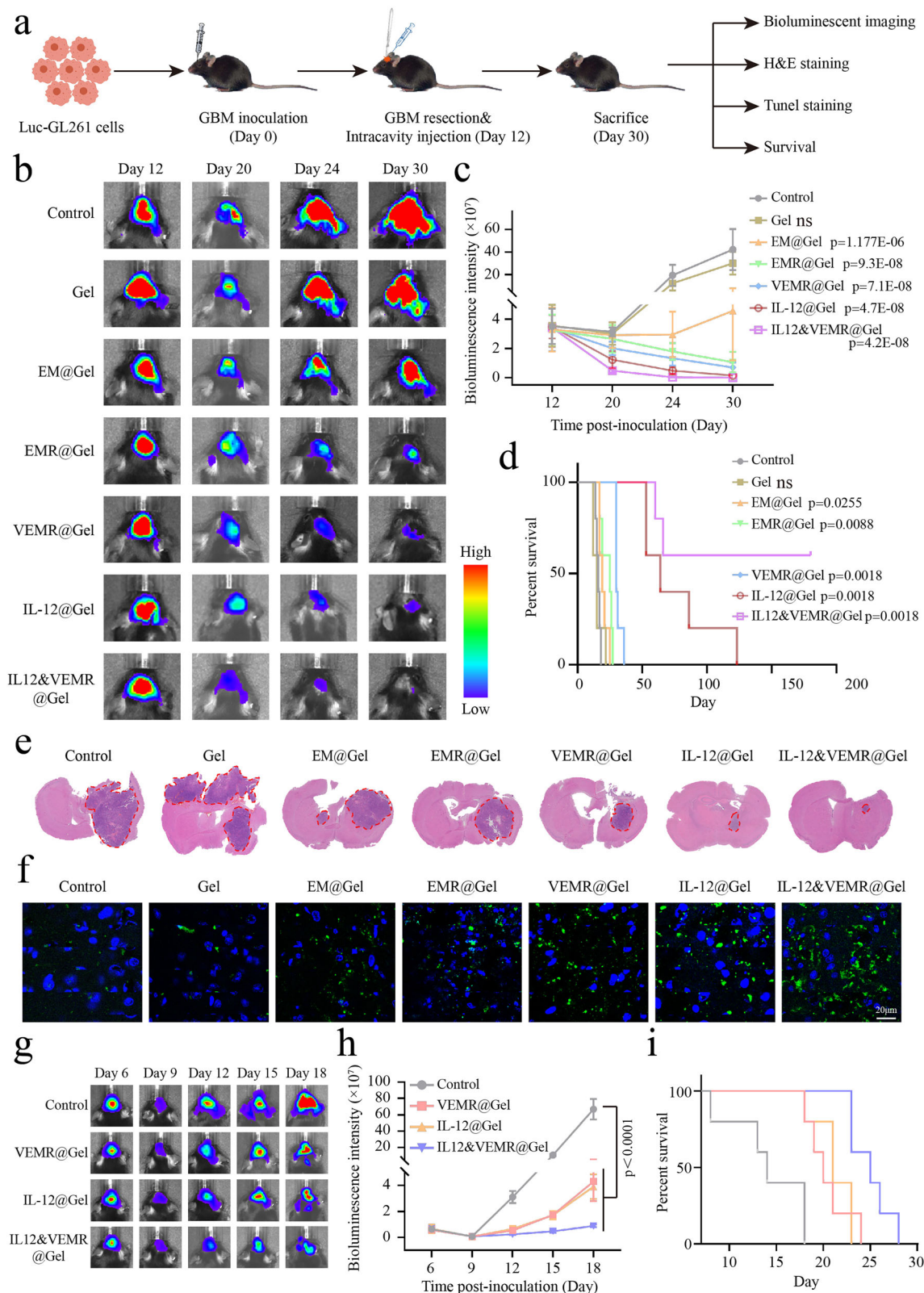
Fig. 7 | In vivo therapy of exo-gel delivery system. a Timeline schematic of the animal experiment. **b** Luminescence images of orthotopic Luc-GL261 GBM tumor-bearing mice following different treatments monitored on day 12, 20, 24 and 30. **c** Quantified signal intensity of (**b**) (*n* = 5 mice per group). Two-way ANOVA test was applied. Data are presented as mean ± SEM. **d** Survival analysis of mice in each group (*n* = 5 mice per group). **e** Representative H&E images of the orthotopic GBM tumors after the indicated treatments. **f** TUNEL staining of brain tissue sections obtained from mice tumors after treatments. **g** Luminescence images of orthotopic Luc-CT2A GBM tumor-bearing mice following different treatments monitored on day 6, 9, 12, 15 and 18. **h** Quantified signal intensity of (**g**) (*n* = 5 mice per group). Two-way ANOVA test was applied. Data are presented as mean ± SEM. **i** Survival analysis of orthotopic Luc-CT2A GBM tumor-bearing mice in each group (*n* = 5 mice per group).

growth. On the 6th day after inoculation with Luc-CT2A cells, the brain tumors were surgically removed. Mice were randomly divided into four groups (control, VEMR@Gel, IL-12@Gel, and IL-12&VEMR@Gel), and the multifunctional exo-gel delivery systems were injected into the resection cavity. IL-12&VEMR@Gel significantly inhibited tumor growth and prolonged the survival of the mice (Fig. 7g–i). In summary, these results demonstrated the excellent ability of IL-12&VEMR@Gel to suppress glioma recurrence.

Antitumor immune response of exo-gel delivery system on glioma relapse model

Encouraged by the satisfactory antitumor effects of IL-12&VEMR@Gel, immune activation was assessed in vivo. On the 30th day, the mice were euthanized, and brain tumor tissues were harvested to prepare a single-cell suspension via Percoll cell isolation solution. The immune cells were stained and analyzed using FCM to evaluate the overall changes in immune cells within the tumor microenvironment. Quantitative FCM results (Fig. 8b–f) revealed that after IL-12&VEMR@Gel treatment, the proportions of mature DCs (CD80$^+$CD86$^+$), CD8$^+$ T cells (CD3$^+$CD8$^+$), and activated T cells (CD25$^+$CD69$^+$) in the GBM lesions of tumor-bearing mice significantly increased, whereas the proportions of Treg cells (CD4$^+$Foxp3$^+$) and MDSCs (CD11b$^+$Gr-1$^+$) notably decreased. This finding indicated a broad reversal of the immunosuppressive microenvironment in GBM after injecting IL-12&VEMR@Gel into the intracavity, which is a crucial step in antitumor immunity. Given that changes in the types and numbers of immune cells in the tumor microenvironment can lead to alterations in cytokine levels, an enzyme-linked immunosorbent assay (ELISA) was used to evaluate the expression of relevant cytokines at the tumor site. After treatment, the IL-12&VEMR@Gel group exhibited the highest levels of interferon-γ (IFN-γ) and tumor necrosis factor-α (TNF-α), which are closely related to the antitumor effect of CD8$^+$ T cells and the activation of T cells. In contrast, the levels of interleukin-4 (IL-4) and interleukin-10 (IL-10), which are associated with the maintenance of the immunosuppressive characteristics of the tumor microenvironment, were the lowest (Fig. 8g–j). These results further confirm that IL-12&VEMR@Gel comprehensively and thoroughly activated the antitumor immune response within the brain, resulting in the transformation of GBM from a "cold" tumor to a "hot" tumor.

To explore whether the treatments affected the GICs, the expression of CD133 and Notch1 in the tumor-bearing brains of each group was detected through immunofluorescence and Western blotting. As shown in Fig. S16a, numerous green fluorescence signals were observed in the control and Gel groups, and small amounts of green fluorescence signals appeared in the EM@Gel group, EMR@Gel group, and VEMR@Gel group; the green fluorescence signals were the lowest in the IL-12&VEMR@Gel group. Similarly, red fluorescence signals were significantly attenuated in the IL-12&VEMR@Gel group compared with the control group. Western blotting results shown in Fig. S16b were similar to those mentioned above, and the expression levels of Notch1 and CD133 in the IL-12&VEMR@Gel group were significantly lower. These results indicated that IL-12&VEMR@Gel could significantly inhibit the expression of Notch1 and CD133, which is crucial for inhibiting the recurrence of brain glioma. In conclusion, the injection of a multifunctional exo-hydrogel system into the resection cavity of postoperative GBM mice not only inhibited the stemness of GICs and killed GICs but also reversed the immunosuppressive microenvironment, and thus effectively inhibited GBM recurrence.

Discussion

GBM, one of the most aggressive primary brain tumors, has an exceedingly low 5-year survival rate and a high risk of recurrence. This inevitable recurrence is driven primarily by residual GICs and the immunosuppressive microenvironment[32]. Therefore, targeting and treating GICs in situ after surgery, as well as reversing the immunosuppressive microenvironment are promising strategies for suppressing GBM recurrence. Here, an injectable IL-12&VEMR@Gel was designed to locally deliver therapeutic agents into the GBM resection cavity for postoperative in situ targeting and killing of GICs and reversal of the immunosuppressive microenvironment to prevent GBM relapse. The in vitro results demonstrated that VEMR significantly suppressed GIC and glioma cell proliferation and promoted their apoptosis. In mouse GBM resection models, IL-12&VEMR@Gel, with notable inhibition of the stemness of GICs and excellent antitumor immune responses, significantly suppressed tumor recurrence and prolonged the survival time of mice.

As a pivotal factor for GBM recurrence, GICs are insensitive to current clinical treatments, and there are no clinically approved medications specific for GICs[33,34]. In this study, ^{D}VAP peptides were modified on the surface of exos by click chemistry to enhance the targeting of residual GICs and glioma cells[35,36]. Lu et al. reported that the ^{D}VAP peptides exhibited excellent binding affinity for GRP78, making it a promising candidate for targeting GICs[37]. GRP78, a member of the heat shock protein 70 family, is lowly expressed in normal cells but highly high expressed in GICs and glioma cells. Our results showed that VEMR exhibited favorable targeting characteristics toward U87 GICs and U87 cells and could better promote the cellular uptake of MIT and siRNAs (Fig. 3), which was a critical factor in GIC-targeted treatments. Additionally, we found that VEMR with a remarkable tropism toward GBM cells significantly suppressed the proliferation of GICs and glioma cells, promoted their apoptosis in vitro (Figs. 5 and S9–S12); moreover, simultaneous intratumoral administration of VEMR and IL-12 effectively suppressed glioma progression in mouse GBM models (Fig. 6), along with good biocompatibility in vivo (Fig. S14). Studies have confirmed that Notch1 is frequently activated in GICs and is crucial for regulating their growth, stemness and self-renewal, suppressing Notch1 activity diminishes the stem cell properties of GICs and affects their proliferative capabilities[38,39]. In this work, we discovered that siNotch1 loading into exos could downregulate the expression of Notch1 at mRNA and protein levels (Fig. 5a–c), and VEMR significantly reduced the expression of Notch1 and CD133 in GICs and in vivo to decrease the stem cell properties of GICs (Figs. 5f; S13 and S16a, b). Furthermore, the combination of siNotch1 and MIT in VEMR effectively targeted and killed GICs and glioma cells (Figs. 3 and 5). Taken together, the combination of siNotch1 and MIT reduced the stemness of GICs and killed GICs, thereby inhibiting GBM recurrence.

The immunosuppressive tumor microenvironment, one of the primary contributors to GBM recurrence, facilitates immune escape by modulating the infiltration of antitumor immune cells; hence, remodeling the immunosuppressive tumor microenvironment is also critical for suppressing GBM recurrence[40–42]. Our findings revealed that the local delivery of VEMR and IL-12 via the hydrogel system substantially reduced tumor relapse and extended the survival of mice following surgical removal (Fig. 7). The effects of MIT on ICD can trigger damage-associated molecular patterns and facilitate the maturation of DC cells[43]. In our work, compared with control and Gel groups, the number of DC cells in the groups containing MIT (EM@Gel, EMR@Gel, VEMR@Gel, IL-12&VEMR@Gel) increased (Fig. 8c). Notably, the numbers of DCs, CD8$^+$ T cells and activated T cells were highest in IL-12&VEMR@Gel group (which included both IL-12 and MIT), whereas the numbers of Treg cells and MDSCs were lowest (Fig. 8). Moreover, the levels of IFN-γ and TNF-α in IL-12&VEMR@Gel group significantly increased, whereas the levels of IL-4 and IL-10 significantly decreased, suggesting a synergistic effect of IL-12 with MIT in promoting immune cell infiltration and activating the immune system, thus reversing the immunosuppressive microenvironment. Notably, the therapeutic efficacies of IL-12 and IL-12&VEMR were comparable in the primary-tumor model, however, in the postoperative resection model, IL-12&VEMR@Gel exhibited a markedly amplified antitumor effect than
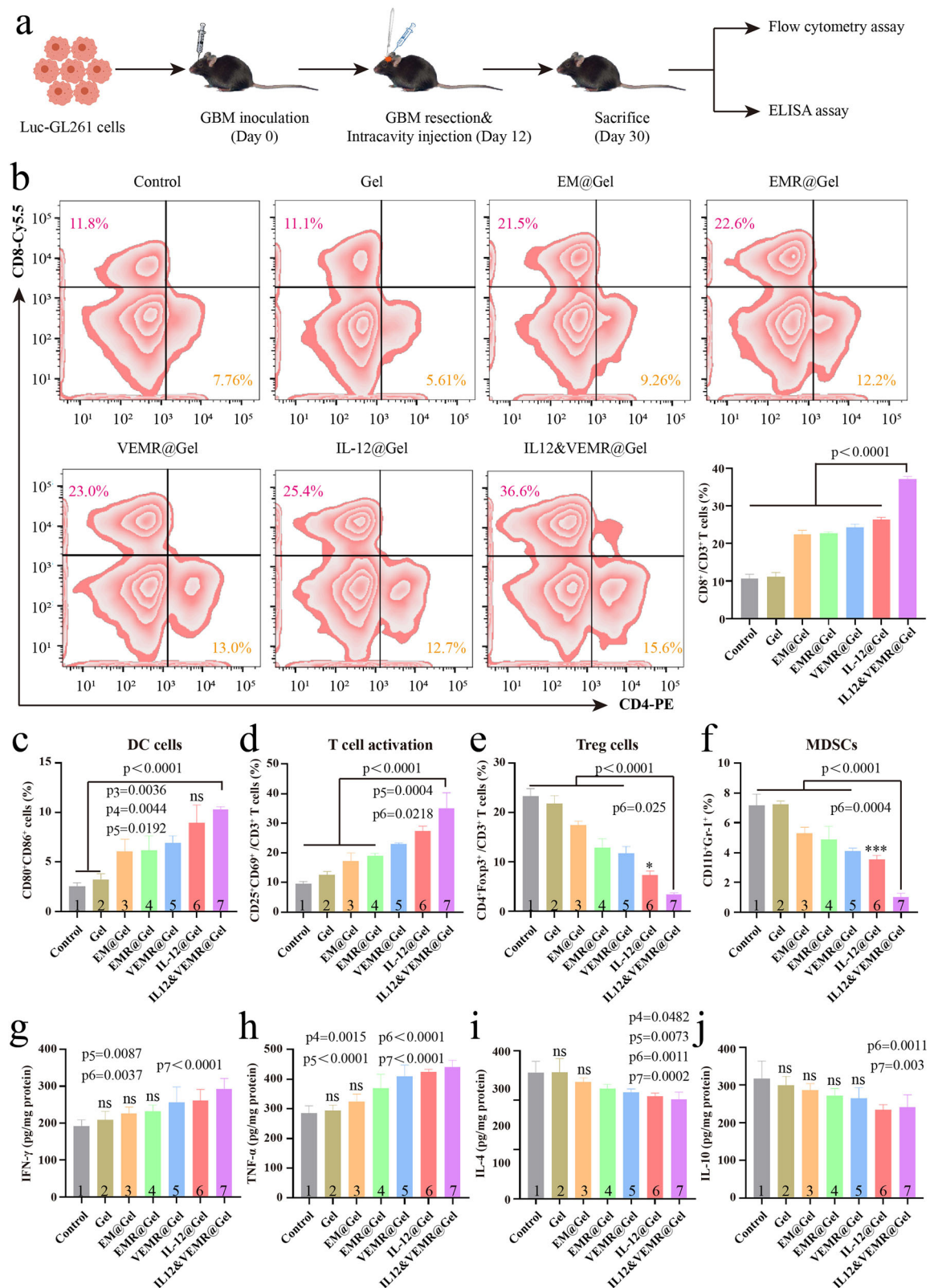
Fig. 8 | The evaluation of antitumor immune response in GL261 postresection glioma-bearing brain tissue. a Schematic diagram of the experimental design. **b** Representative FCM contour plots of T cells in each group and quantification of CD8+ T cells ($n = 3$ mice per group). One-way ANOVA test was applied. Data are presented as mean ± SD. **c–f** Quantification results of the proportion of DC cells (**c**),

T cell activation (**d**), Treg cells (**e**), and MDSCs (**f**) in tumor-bearing brain tissues of each group ($n = 3$ mice per group). One-way ANOVA test was applied. Data are presented as mean ± SD. **g–j** ELISA quantification results of IFN-γ (**g**), TNF-α (**h**), IL-4 (**i**), and IL-10 (**j**) in tumor-bearing brain tissues ($n = 5$ mice per group). One-way ANOVA test was applied. Data are presented as mean ± SD.

of IL-12@Gel in both GL261 and CT2A recurrent model, underscoring the pivotal contribution of GICs to recurrence. Herein, the combined administration of IL-12 and VEMR can not only inhibit GICs but also reshape the immunosuppressive microenvironment, thereby synergistically preventing GBM relapse.

The standard clinical therapeutic approach for GBM involves surgical removal of tumors, after which TMZ treatment and/or radiation therapy are administered following a several-week recovery interval[44]. In addition, emerging adjunctive therapies such as tumor electrical field therapy (TTF), Gliovac™, and oncolytic viruses are used to treat GBM[45–47]. Nevertheless, incomplete surgical removal of the tumor, resistance to chemotherapy and radiotherapy, poor patient compliance and limited targeting ability for postoperative microscopic residual TTF lesions, the small scale of clinical trials for Gliovac™, and systemic inflammatory toxicities of oncolytic viruses all contribute to the difficulty in curing GBM. This study focused on two core factors that induce GBM recurrence, namely, GICs and the immunosuppressive microenvironment, and a multifunctional exo-gel in situ delivery system loaded with MIT, siNotch1, and IL-12 was developed. When injected postoperatively into the resection cavity, this system could target and eliminate residual GICs and glioma cells, and suppress GIC stemness while activating antitumor immune responses, thereby inhibiting GBM relapse. In summary, IL-12&VEMR@Gel could eradicate residual GICs and glioma cells and reverse the immunosuppressive microenvironment to prevent postoperative GBM recurrence. Such a strategy has the potential to enhance synchronization with clinical surgical practices and may offer broad clinical applications for targeting residual GICs after surgical intervention.

Methods

Cell culture

U87 (CL-0238), U251 (CL-0237) cells were acquired from Procell Life Science and Technology Co., Ltd. (Wuhan, China), GL261 (BNCC341792), Luc-GL261 (BNCC337638), HA1800 cells (BNCC340443) were purchased from Beina Chuanglian Biotechnology Institute (Beijing, China), CT2A (BFN60810497) cells were obtained from Bluefbio Biology Technology Development Co., Ltd. (Shanghai, China), Luc-CT2A cells were constructed by GenCefe Biotech Co., Ltd. (Jiangsu, China), and RAW 264.7 cells were generously provided by Jingwen Zhao, Tianjin Medical University General Hospital. All cell lines were authenticated by short tandem repeat (STR) profiling and routinely tested to confirm the absence of mycoplasma contamination. All the cell lines were cultured in DMEM medium (Gibco, USA) supplemented with 10% fetal bovine serum (FBS, Vivacell, Germany) and 1% penicillin-streptomycin (Invitrogen, USA) at 37 °C under a 5% CO_2 atmosphere.

CD133$^+$ GICs were isolated using magnetic-activated cell sorting (MACS). Following a 7-day culture period, tumor spheres were harvested by centrifugation and then resuspended in serum-free DMEM/F12 medium to adjust the cell concentration (1×10^5 cells/μL) to minimize serum interference. A mixture containing 200 μL cell suspension, 40 μL FcR blocking reagent, and 40 μL CD133 microbeads was prepared in PBS buffer supplemented with 5% FBS and 2 mM EDTA. After thorough mixing, the mixture was incubated at 4 °C for 15 min. The labeled cell suspension was then loaded onto a pre-assembled magnetic separation column. Unbound cells were removed by washing three times with 500 μL buffer. After removing the column from the magnetic field, CD133$^+$ labeled cells (GICs) were obtained and subsequently cultured in stem cell medium consisting of DMEM/F12 supplemented with EGF (20 ng/mL, PeproTech), bFGF (20 ng/mL, PeproTech), and B27 supplement (1:50; Invitrogen, USA). GICs were characterized by Western blotting and immunofluorescence assays.

Isolation and characterization of exos

Exos were isolated from RAW 264.7 cell culture supernatant[48]. In brief, the supernatant was collected and subjected to sequential centrifugation at $2000 \times g$ (20 min) and $10{,}000 \times g$ (30 min) at 4 °C to remove dead cells and cell debris. The supernatant from the previous step was subsequently filtered through a 0.22 μm membrane and ultracentrifuged (Beckman Optima L-100 XP, Beckman Coulter) at $100{,}000 \times g$ (70 min). Afterward, the pelleted exos were obtained and resuspended in sterilized PBS, and the protein concentration was quantified using a BCA assay and preserved at −80 °C for subsequent experiments. The particle size and morphological characteristics were evaluated through NTA (Particle Metrix PMX, Germany) as well as TEM (Hitachi HT7700, Japan). Additionally, the presence of exo-specific markers such as CD9, CD63 and TSG101 was confirmed by western blotting.

Preparation and characterization of the exo delivery system

The exo surfaces were modified with ^{D}VAP peptides through the application of click chemistry. First, DBCO-sulfo-NHS ester (Glen Research, VA, USA) was dissolved in DMSO to a concentration of 10 μM, then added to the exos suspension (0.5 mg/mL) prior to incubation at 25 °C for 4 h with gentle mixing. Subsequently, extra DBCO-sulfo-NHS was removed by ultrafiltration to obtain DBCO-Exos, after which ^{D}VAP peptides modified with 5-azidopentanoic acid (Scilight Biotechnology, Beijing, China) were incubated with them at 4 °C overnight. Following the reaction, free ^{D}VAP was removed by ultrafiltration to obtain VE. To verify the successful chemical coupling between the targeted peptides and exos, the exos were modified by the same procedure, and the TAMRA-^{D}VAP-Exos were characterized by FCM.

Synthetic siRNAs targeting specific genes were designed based on the sequences described in Table S2, and produced by GenePharma Co. Ltd (Shanghai, China). Transfection of siRNAs into exos was performed using the Exo-fect™ Exosome Transfection Reagent (System Biosciences, CA, USA) according to the manufacturer's protocol. Briefly, ^{D}VAP-Exo, MIT (mitoxantrone dihydrochloride, Med Chem Express, USA) and siRNAs (GenePharma, Shanghai, China) were mixed at a mass ratio of 10:8:1. An appropriate volume of Exo-fect was introduced, and the mixture was incubated at 37 °C for 20 min. ExoQuick-TC reagent was subsequently added, and this mixture was allowed to react on ice for 30 min, after which the reaction was stopped. Afterward, the mixture was centrifuged at $12{,}000 \times g$ for 3 min, and ^{D}VAP-Exo/MIT/siRNA (VEMR) was obtained and resuspended in PBS. The particle size and morphological characteristics were assessed through NTA and TEM.

Drug encapsulation efficiency

To determine the content of MIT in the VEMR, a UV–vis spectrophotometer was employed to measure the absorbance at 627 nm. The standard curve of MIT was shown in Fig. S17, and the encapsulation efficiency of MIT was calculated by the following formula: encapsulation efficiency (%) = $M_E/M_I \times 100\%$, where M_E represents the mass of MIT encapsulated in the exo delivery system, and M_I represents the original mass of MIT. Similarly, siRNAs were labeled with Cy3 (Ex = 530 nm, Em = 570 nm), and the encapsulation efficiency of the siRNA in VEMR was detected via a microplate reader.

Drug stability

To investigate the stability of the siRNA in exos, free siRNA or EMR with or without 0.5% Triton X-100 was coincubated with RNase A at 37 °C for a specific duration, and the degradation of the siRNA was analyzed by agarose gel electrophoresis.

The in vitro release profile of MIT from VEMR was further evaluated in PBS at pH 7.4 and 5.5 using a dynamic dialysis method. Adequate volumes of sample solutions were swiftly transferred into dialysis bags with a molecular weight cutoff ranging from 8 to 12 kDa, and subsequently dialyzed with 50 mL of PBS. The released MIT was quantified at 627 nm by a UV–Vis spectrophotometer at regular intervals.

Targeting and cellular uptake of the exo delivery system

Exos, VE and VEMR were marked with DiI. In short, HA1800 cells, U87 cells and U87 GICs were seeded in confocal dishes, and when the cells density reached approximately 80%, exos, VE and VEMR (5 μg) were added to the dishes and incubated for 4 h. Following incubation, cells were washed with PBS, fixed with 4% paraformaldehyde, and stained with DAPI. Subsequently, these cells were observed by CLSM to examine the fluorescence intensity of the DiI-labeled exos. Additionally, to investigate the effect of receptor blocking on targeting in this system, HA1800 cells, U87 cells and U87 GICs were incubated with ^{D}VAP peptides for 1 h, VE was added, and the intracellular fluorescence intensity was detected by CLSM.

When the cell density reached approximately 80%, different formulations (PBS, Cy3-labeled siRNA, MIT, EMR, and VEMR) were added for coincubation with U87 cells and U87 GICs for 4 h, after which the cellular uptake of the exo delivery system was observed by CLSM.

To explore the underlying uptake mechanism of this system by U87 cells and U87 GICs, the cells were pre-incubated for 1 h with various endocytic inhibitors (50 μM amiloride hydrochloride, 5 mM methyl-β-cyclodextrin (M-β-CD), 10 μg/mL chlorpromazine and 80 μM dynasore), followed by the addition of DiI-VE and further incubation for 2 h. In addition, to evaluate temperature-dependent uptake, another group of cells was incubated at 4 °C for 2 h. The intracellular fluorescence intensity was subsequently detected by CLSM.

Lyso/endosome escape assay

To detect lyso/endosome escape of siRNA and MIT, U87 cells and U87 GICs were seeded and cultured in a confocal dish, and treated with VEMR (Cy3-labeled siRNA) for 2, 4 and 8 h at 37 °C. LysoTracker Green was used to mark lyso/endosomes, Hoechst 33342 was used to label nuclei, and lyso/endosomal escape was observed by CLSM.

Cytotoxicity assay

The cytotoxicity of exos and MIT on U87 and HA1800 cells was evaluated using a CCK-8 assay. Briefly, cells were seeded in 96-well plates and treated with various concentrations of exos and formulations for 48 h. Subsequently, CCK-8 reagent was added to each well, followed by incubation for the designated duration. The absorbance at 450 nm was measured using a microplate reader.

Cell proliferation assay

U87 cells, U251 cells, GL261 cells, CT2A cells, U87 GICs, U251 GICs, GL261 GICs, and CT2A GICs were seeded in 96-well plates, and PBS, MIT, VE, VER, VEM, and VEMR were added. After 48 h of incubation, cellular proliferation in different experimental samples was detected by a CCK-8 assay.

Apoptosis assay

The apoptosis of U87 cells, U251 cells, GL261 cells, CT2A cells, U87 GICs, U251 GICs, GL261 GICs, and CT2A GICs was detected by FCM after different treatments. Cells were plated in 6-well plates and treated with different experimental formulas (PBS, MIT, VE, VER, VEM, or VEMR). Following a 36-h incubation period, cells were harvested and stained using an Annexin V-APC/DAPI Apoptosis detection kit according to the manufacture's protocol, and the cells subsequently assessed by a BD Accuri C6 flow cytometer.

Gene expression assay

After U87 GICs were treated with different samples (PBS, free siNotch1, Lipo/siNotch1, VER) for 48 h, total RNA was extracted utilizing TRIzol reagent and reverse transcribed to cDNA by RTase according to the manufacturer's guidelines (Tiangen Biochemical Technology Co., Ltd., Beijing, China). Primer sequences used for reverse transcription were provided in Table S3. Afterward, cDNA (1 μL) was added to the PCR system with forward and reverse primers (1 μL), and the reaction

volume was supplemented with DEPC-treated water. The amplification process of this reaction system involved heating to 95 °C for 15 s, followed by annealing/extension at 60 °C for 1 min, which was repeated for a total of 40 cycles. Actin served as a housekeeping gene, and Notch1 expression was estimated via the $2^{-\Delta\Delta CT}$ method.

Western blotting analysis

RIPA buffer supplemented with phenylmethanesulfonylfluoride (PMSF) (Solarbio Biotechnology, Beijing, China) was used to lyse exos, RAW264.7 cells, U87 cells, U87 GICs, GL261 GICs or mouse brain tumor tissues. Protein samples were denatured by boiling at 100 °C for 5 min after mixing with 5× loading buffer. Subsequently, proteins including CD9 (sc-13118, Santa Cruz biotechnology, USA), CD63 (sc-5275, Santa Cruz biotechnology, USA), TSG101 (sc-7964, Santa Cruz biotechnology, USA), Notch1 (10062-2-AP, Proteintech, USA), CD133 (18470-1-AP, Proteintech, USA), Nestin (sc-58813, Santa Cruz biotechnology, USA), and Hes1 (sc-166410, Santa Cruz biotechnology, USA) proteins were separated using 10% SDS–PAGE. The membranes were immunoblotted overnight at 4 °C with the following primary antibodies: anti-CD9 (1:1000), anti-CD63 (1:1000), anti-TSG101 (1:1000), anti-Notch1 (1:200), anti-CD133 (1:200), anti-Nestin (1:200), anti-Hes1 (1:200) and anti-β-actin (1:1000). After incubation with horseradish peroxidase-conjugated secondary antibodies (1:5000) for 1 h at room temperature, protein bands were detected via a chemiluminescence reagent and analyzed on a C-DiGit (LICOR Corporation, USA).

Preparation and characterization of the exo-gel delivery system

Two percent chitosan (CS) acetic acid solution (dissolved in acetic acid solution), 56% β-glycerophosphate (β-GP) sodium solution (dissolved in NaHCO₃ solution) and 0.5% gelatin (GA) solution (dissolved in acetic acid solution) were prepared. In accordance with the volume ratio (CS: β-GP: GA = 10:2:0.25), CS and GA were mixed first, and then β-GP was added under stirring conditions; subsequently, the pH was adjusted to 7.4, and a temperature-sensitive hydrogel (gel) was obtained. VEMR and/or recombinant murine IL-12 (Protech Systems Co., Ltd., USA) was added to the gel. The temperature-sensitive properties of the gels were detected at 4 °C and 37 °C. The morphology of the gel in the freeze-dried state was characterized through SEM, and the rheology of the gel was detected via a rheometer. Moreover, the gel's biocompatibility was evaluated by a hemolysis test; when the hemolysis rate of a sample is less than 5%, it meets medical material requirements. Moreover, the exos released from the gel were assessed. Exos were labeled with DiI, then loaded into the gel, and the artificial cerebrospinal fluid was used as the release medium. 3D layer scanning was performed via a laser confocal microscope at 0 h and 24 h to observe the release of exos.

Establishment of the GBM model and antitumor efficacy study in vivo

Male C57BL/6 mice (5–6 weeks old, 18–20 g) were obtained from the China Food and Drug Research Institute and used to establish the GBM model. For the GL261 orthotopic models, a suspension of Luc-GL261 cells (5×10^5 cells in 10 μL serum-free medium) was stereotactically injected into the right frontal lobe of mice at coordinates 1.0 mm anterior and 2.0 mm lateral to the bregma, and 3.5 mm deep. Following a 12-day period, mice were randomly assigned to eight groups, as follows: PBS, MIT, VE, VER, VEM, VEMR, IL-12, IL-12&VEMR. Subsequently, the mice were subjected to intratumor injection with the formulations (10 μL containing dosages of 3 mg/kg for MIT, 0.375 mg/kg for siRNA, and 50 μg/kg for IL-12) mentioned above. Bioluminescence imaging was carried out on day 12, 16, 18 and 21. On the 21st day, the brain tumor was excised for the TUNEL assay. On day 21, some mice were sacrificed, blood was collected for hematologic analysis, and vital organ pathological examinations were conducted to evaluate the in vivo biocompatibility of the delivery system.

Following the successful establishment of the postoperative GBM model, mice were randomized into seven groups at random as follows: control, gel, EM@Gel, EMR@Gel, VEMR@Gel, IL-12@Gel, and IL-12&VEMR@Gel. On day 12, after C57BL/6 mice were inoculated with Luc-GL261cells, a high-speed ring knife drill was used to remove a tiny proportion of the circle, whose diameter was approximately 4 mm, from the skull of every mouse in the GBM mouse models described above, and surgical resection of the GBM was performed[49]. Various hydrogels (10 μL containing dosages of 3 mg/kg for MIT, 0.375 mg/kg for siRNA, and 50 μg/kg for IL-12) were subsequently injected into the resection cavity of the mice. Bioluminescence imaging was carried out on day 12, 20, 24 and 30. On the 30th day, the brain tumor bumps were excised for the TUNEL assay. On day 30, some mice were euthanized, and brain tissues were harvested for subsequent H&E staining to detect tumor growth, immunofluorescence, Western blotting and FCM were utilized to detect the expression of CD133 and Notch1, along with the infiltration of immune cells (CD4, CD8, DCs, Treg cells, and MDSCs).

For the CT2A orthotopic models, a Luc-CT2A serum-free cell suspension, containing 3×10^5 cells in 10 μL, was stereotactically injected into the right frontal lobe of mice (1.0 mm anterior, 2.0 mm lateral to the bregma at 3.5 mm depth) via stereotactic surgery. After the orthotopic models were successfully constructed, the mouse brain tumors were surgically removed on the 6th day, and divided into four groups at random as follows: control, VEMR@Gel, IL-12@Gel, and IL-12&VEMR@Gel. Bioluminescence imaging was carried out on day 6, 9, 12, 15 and 18.

FCM and cytokine analysis

GBM mice were perfused with saline, and the mouse brain tumor tissues were collected. Then, the brain tumor tissues were gently ground on a 70 μm cell filter to separate the tissue. After layering on a discontinuous Percoll gradient (30% Percoll above 70% Percoll), the cell suspension was subjected to centrifugation at $1000 \times g$ for 30 min. The middle white annular layer containing the separated cells was collected, followed by wash with PBS and centrifugation at $500 \times g$ and 4 °C for 10 min, and then resuspended in 2% BSA-PBS. The immune cells were stained according to the manufacturer's instructions and analyzed by FCM assays. The following antibody panels were used: anti-CD3-FITC (E-AB-F1013C, Elabscience), anti-CD4-PE (E-AB-F1097D, Elabscience), and anti-CD8-Percp Cy5.5 (E-AB-F1104J, Elabscience) for CD4$^+$/CD8$^+$ T-cell analysis; anti-CD11c-FITC (E-AB-F0991C, Elabscience), anti-CD80-APC (E-AB-F0992E, Elabscience), and anti-CD86-PE (E-AB-F0994D, Elabscience) for DC cell detection; anti-CD3-FITC (E-AB-F1013C, Elabscience), anti-CD25-APC (E-AB-F1102E, Elabscience), and anti-CD69-PE (E-AB-F1187D, Elabscience) for T-cell activation assessment; anti-CD3-Percp Cy5.5 (E-AB-F1013J, Elabscience), anti-CD4-FITC (E-AB-F1353C, Elabscience), and anti-Foxp3-PE (E-AB-F1238D, Elabscience) for Treg cell analysis; and anti-CD11b-FITC (E-AB-F1081C, Elabscience) and anti-Gr-1-PE (E-AB-F1120D, Elabscience) for MDSC detection. The secretion levels of IFN-γ (E-EL-M0048c), TNF-α (E-EL-M3063), IL-4 (E-EL-M0043c), and IL-10 (E-EL-M0046c) in brain tumor tissues were determined by ELISA (Elabscience).

Statistics and reproducibility

All statistical analyses were performed using GraphPad Prism 8.0.2 software. The experiments were performed independently, and each group was repeated at least three times. The sample number "n" indicated in the figure legends, and the data were presented as the mean ± SD or SEM. Student's t test or ANOVA was used for group comparison, a p-value of less than 0.05 was considered statistically significant ($^*p < 0.05$, $^{**}p < 0.01$, $^{***}p < 0.001$, $^{****}p < 0.0001$).

Ethics statement

All experimental procedures involving animals were performed in accordance with the Guidelines for the Care and Use of Laboratory Animals and approved by the Animal Ethics Committee of Tianjin Medical University (TMUa MEC 2021001). At no point did we exceed the approved limits for tumor size/burden in our animal experiments.

Reporting summary

Further information on research design is available in the Nature Portfolio Reporting Summary linked to this article.

Data availability

The data are available within the article, Supplementary Information or Source data file. Source data are provided with this paper.

References

1. Wang, G. & Wang, W. Advanced cell therapies for glioblastoma [J]. *Front. Immunol.* **13**, 904133–904149 (2022).
2. Zhang, P., Zhang, Y. & Ji, N. Challenges in the treatment of glioblastoma by chimeric antigen receptor T-cell immunotherapy and possible solutions [J]. *Front. Immunol.* **13**, 927132–927145 (2022).
3. Tseng, C. L. et al. Evolving concepts in margin strategies and adaptive radiotherapy for glioblastoma: a new future is on the horizon [J]. *Neuro Oncol.* **26**, S3–S16 (2024).
4. So, J. S., Kim, H. & Han, K. S. Mechanisms of invasion in glioblastoma: extracellular matrix, Ca(2+) signaling, and glutamate [J]. *Front. Cell. Neurosci.* **15**, 663092–663102 (2021).
5. Pan, T. et al. Glioma-stem-cell-derived exosomes remodeled glioma-associated macrophage via NEAT1/miR-125a/STAT3 pathway [J]. *Cancers* **16**, 2500–2518 (2024).
6. Bastiancich, C. et al. Injectable nanomedicine hydrogel for local chemotherapy of glioblastoma after surgical resection [J]. *J. Control. Release* **264**, 45–54 (2017).
7. Wang, Z. et al. Silk microneedle patch capable of on-demand multidrug delivery to the brain for glioblastoma treatment [J]. *Adv. Mater.* **34**, e2106606–e2106618 (2022).
8. Bozzato, E. et al. Dual-drug loaded nanomedicine hydrogel as a therapeutic platform to target both residual glioblastoma and glioma stem cells [J]. *Int. J. Pharm.* **628**, 122341–122353 (2022).
9. Agosti, E. et al. Glioma stem cells as promoter of glioma progression: a systematic review of molecular pathways and targeted therapies [J]. *Int. J. Mol. Sci.* **25**, 7979–8002 (2024).
10. Ramar, V. et al. Progress in glioma stem cell research [J]. *Cancers* **16**, 102–130 (2023).
11. Yi, L. et al. Notch1 signaling pathway promotes invasion, self-renewal and growth of glioma initiating cells via modulating chemokine system CXCL12/CXCR4 [J]. *J. Exp. Clin. Cancer Res.* **38**, 339–354 (2019).
12. Sun, Z. et al. Glioblastoma stem cell-derived exosomes enhance stemness and tumorigenicity of glioma cells by transferring Notch1 protein [J]. *Cell. Mol. Neurobiol.* **40**, 767–784 (2020).
13. Yin, J. et al. Hypoxanthine phosphoribosyl transferase 1 metabolizes temozolomide to activate AMPK for driving chemoresistance of glioblastomas [J]. *Nat. Commun.* **14**, 5913–5928 (2023).
14. Datta, S. et al. Repurposing FDA approved drugs inhibiting mitochondrial function for targeting glioma-stem like cells [J]. *Biomed. Pharmacother.* **133**, 111058–111083 (2021).
15. Wang, R. et al. Tumor microenvironment-responsive micelles assembled from a prodrug of mitoxantrone and 1-methyl tryptophan for enhanced chemo-immunotherapy [J]. *Drug Deliv.* **30**, 2182254–2182266 (2023).
16. Gabel, M. et al. Surface design options in polymer- and lipid-based siRNA nanoparticles using antibodies [J]. *Int. J. Mol. Sci.* **23**, 13929–13951 (2022).
17. Arya, S. B., Collie, S. P. & Parent, C. A. The ins-and-outs of exosome biogenesis, secretion, and internalization [J]. *Trends Cell Biol.* **34**, 90–108 (2024).
18. Paskeh, M. D. A. et al. Emerging role of exosomes in cancer progression and tumor microenvironment remodeling [J]. *J. Hematol. Oncol.* **15**, 83–122 (2022).

19. Wang, X. et al. Non-immunogenic, low-toxicity and effective glioma targeting MTI-31 liposomes [J]. *J. Control. Release* **316**, 381–392 (2019).

20. Lin, H. et al. Understanding the immunosuppressive micro-environment of glioma: mechanistic insights and clinical perspectives [J]. *J. Hematol. Oncol.* **17**, 31–112 (2024).

21. Codrici, E. et al. Friends with benefits: chemokines, glioblastoma-associated microglia/macrophages, and tumor microenvironment [J]. *Int. J. Mol. Sci.* **23**, 2509–2545 (2022).

22. Jones, D. S. et al. Cell surface-tethered IL-12 repolarizes the tumor immune microenvironment to enhance the efficacy of adoptive T cell therapy [J]. *Sci. Adv.* **8**, eabi8075–eabi8092 (2022).

23. Kaczanowska, S. et al. Genetically engineered myeloid cells rebalance the core immune suppression program in metastasis [J]. *Cell* **184**, 2033–2052 (2021).

24. Liu, M. et al. Inhalable extracellular vesicle delivery of IL-12 mRNA to treat lung cancer and promote systemic immunity [J]. *Nat. Nanotechnol.* **19**, 565–575 (2024).

25. Wang, X. et al. In situ targeting nanoparticles-hydrogel hybrid system for combined chemo-immunotherapy of glioma [J]. *J. Control. Release* **345**, 786–797 (2022).

26. Kunigelis, K. E. & Vogelbaum, M. A. Therapeutic delivery to central nervous system [J]. *Neurosurg. Clin. N. Am.* **32**, 291–303 (2021).

27. Padmakumar, S. & Amiji, M. M. Long-acting therapeutic delivery systems for the treatment of gliomas [J]. *Adv. Drug Deliv. Rev.* **197**, 114853–114884 (2023).

28. Bastiancich, C. et al. Rationally designed drug delivery systems for the local treatment of resected glioblastoma [J]. *Adv. Drug Deliv. Rev.* **177**, 113951–113978 (2021).

29. Kawaguchi, Y. et al. Unmanageable cerebrospinal fluid leakage with eosinophilic meningitis in a gliadel wafer implant patient [J]. *Cureus* **16**, e59718–e59724 (2024).

30. Almajidi, Y. Q. et al. Advances in chitosan-based hydrogels for pharmaceutical and biomedical applications: a comprehensive review [J]. *Int. J. Biol. Macromol.* **253**, 127278–127293 (2023).

31. Lee, I. Y. et al. Autologous cell immunotherapy (IGV-001) with IGF-1R antisense oligonucleotide in newly diagnosed glioblastoma patients [J]. *Future Oncol.* **20**, 579–591 (2024).

32. Sheu, M. L. et al. Potential therapeutic effects of thiazolidinedione on malignant glioma [J]. *Int. J. Mol. Sci.* **23**, 13510–13530 (2022).

33. Zhang, X. et al. MELK inhibition effectively suppresses growth of glioblastoma and cancer stem-like cells by blocking AKT and FOXM1 pathways [J]. *Front. Oncol.* **10**, 608082–608096 (2020).

34. Jiang, G. et al. Tailored lipoprotein-like miRNA delivery nanostructure suppresses glioma stemness and drug resistance through receptor-stimulated macropinocytosis [J]. *Adv. Sci.* **7**, 1903290–1903304 (2020).

35. Liu, K., Tsung, K. & Attenello, F. J. Characterizing cell stress and GRP78 in glioma to enhance tumor treatment [J]. *Front. Oncol.* **10**, 608911–608928 (2020).

36. Huang, J. et al. Synthesis and evaluation of [(18)F]AlF-NOTA-c-(D) VAP: a novel PET probe for imaging GRP78 in cancer [J]. *Mol. Pharm.* **21**, 2425–2434 (2024).

37. Wu, S. et al. All-stage targeted therapy for glioblastoma based on lipid membrane coated cabazitaxel nanocrystals [J]. *J. Control. Release* **345**, 685–695 (2022).

38. Tao, Z. et al. Autophagy suppresses self-renewal ability and tumorigenicity of glioma-initiating cells and promotes Notch1 degradation [J]. *Cell Death Dis.* **9**, 1063–1077 (2018).

39. Zhao, G. et al. Targeting EZH2 regulates the biological characteristics of glioma stem cells via the Notch1 pathway [J]. *Exp. Brain Res.* **241**, 2409–2418 (2023).

40. White, J. et al. The tumour microenvironment, treatment resistance and recurrence in glioblastoma [J]. *J. Transl. Med.* **22**, 540–554 (2024).

41. Zhao, L. et al. IGFBP3 induces PD-L1 expression to promote glioblastoma immune evasion [J]. *Cancer Cell Int.* **24**, 60–75 (2024).

42. Li, T. et al. Metabolism/immunity dual-regulation thermogels potentiating immunotherapy of glioblastoma through lactate-excretion inhibition and PD-1/PD-L1 blockade [J]. *Adv. Sci.* **11**, e2310163–e2310177 (2024).

43. Zhang, J. et al. Immunostimulant hydrogel for the inhibition of malignant glioma relapse post-resection [J]. *Nat. Nanotechnol.* **16**, 538–548 (2021).

44. Bastiancich, C. et al. Tailoring glioblastoma treatment based on longitudinal analysis of post-surgical tumor microenvironment [J]. *J. Exp. Clin. Cancer Res.* **43**, 311–336 (2024).

45. Szklener, K. et al. Enhancing glioblastoma treatment through the integration of tumor-treating fields [J]. *Front. Oncol.* **13**, 1274587–1274597 (2023).

46. Raj, D. et al. Pharmacological strategies for improving the prognosis of glioblastoma [J]. *Expert Opin. Pharmacother.* **22**, 2019–2031 (2021).

47. Ling, A. L. et al. Clinical trial links oncolytic immunoactivation to survival in glioblastoma [J]. *Nature* **623**, 157–166 (2023).

48. Pei, X. et al. Targeted exosomes for co-delivery of siFGL1 and siTGF-β1 trigger combined cancer immunotherapy by remodeling immunosuppressive tumor microenvironment [J]. *Chem. Eng. J.* **421**, 129774–129790 (2021).

49. Chen, S. et al. Dual-sensitive drug-loaded hydrogel system for local inhibition of post-surgical glioma recurrence [J]. *J. Control. Release* **349**, 565–579 (2022).

Acknowledgements

Author contributions

H.H. and J.W. conceived and designed the study; M.Z. and M.Y. constructed the formulations, characterization, cell studies and data analysis; M.Z. and R.L. performed animal experiments, data analysis and wrote the manuscript; X.H., J.C., and L.X. helped the animal experiments and facilitated the data and file processing; H.H., Z.B., J.W., S.C., and T.L. further revised the manuscript. All authors discussed the results and commented on the manuscript.

Competing interests

The authors declare no competing interests.

Additional information

Supplementary information The online version contains supplementary material available at https://doi.org/10.1038/s41467-025-67415-y.

Correspondence and requests for materials should be addressed to Jianxin Wang, Bin Zheng or Huining He.

Peer review information *Nature Communications* thanks the anonymous reviewer(s) for their contribution to the peer review of this work. A peer review file is available.

Reprints and permissions information is available at http://www.nature.com/reprints

Publisher's note Springer Nature remains neutral with regard to jurisdictional claims in published maps and institutional affiliations.